A&A 490, 859–871 (2008)
DOI: 10.1051/0004-6361:200809512

Astronomy & Astrophysics

SYMPA, a dedicated instrument for Jovian seismology

II. Real performance and first results

P. Gaulme[1], F. X. Schmider[1], J. Gay[1], C. Jacob[1], M. Alvarez[2], M. Reyes-Ruiz[2], J. A. Belmonte[3], E. Fossat[1], F. Jeanneaux[1], and J.-C. Valtier[1]

[1] Laboratoire FIZEAU, Université de Nice Sophia-Antipolis, CNRS-Observatoire de la Côte d'Azur, 06108 Nice Cedex 2, France
e-mail: Patrick.Gaulme@obspm.fr
[2] Observatorio Astronómico Nacional, Instituto de Astronomía, Universidad Nacional Autónoma de México, Apto. Postal 877, Ensenada, B.C., México
[3] Instituto de Astrofísica de Canarias, Tenerife, Spain

Received 4 February 2008 / Accepted 27 June 2008

ABSTRACT

Aims. SYMPA is the first instrument dedicated to the observation of free oscillations of Jupiter. Its principles and theoretical performance have been presented in Paper I. This second paper describes the data processing method, the real instrumental performance and presents the first results of a Jovian observation run, lead in 2005 at Teide Observatory.
Methods. SYMPA is a Fourier transform spectrometer which works at a fixed optical path difference. It produces Doppler shift maps of the observed object. The velocity amplitude of Jupiter's oscillations is expected to be below 60 cm s^{-1}.
Results. Despite light technical defects, the instrument was demonstrated to work correctly, being limited only by photon noise. A noise level of about 12 cm s^{-1} was reached on a 10-night observation run, with 21% duty cycle, which is 5 time better than similar previous observations. However, no signal from Jupiter is clearly highlighted.

Key words. Sun: helioseismology – instrumentation: interferometers – methods: observational – techniques: spectroscopic – planets and satellites: individual: Jupiter – planets and satellites: formation

1. Introduction

Due to its great mass and its rapid formation, Jupiter has played a crucial role in shaping the Solar System. Two scenarios are generally proposed for the formation of giant planets: the nucleated instability (Safronov & Ruskol 1982) and the gravitational instability models (Cameron 1978; Mayer et al. 2002). An efficient constraint on the formation scenario would be given by measuring the total amount of heavy elements inside Jupiter and the size of the planetary core. Moreover, the knowledge of Jupiter's internal structure would constrain the high pressure hydrogen equation of state, which is still inaccurate, and would particularly solve the question of the nature of the metallic-molecular phase transition (e.g. Guillot et al. 2004). Gudkova & Zharkov (1999) showed that the observation of oscillation modes up to degree $\ell = 25$ would strongly constrain Jupiter's internal structure by exploring both the hydrogen plasma-phase transition and the supposed core level.

Attempts to observe Jovian oscillations have been made since the mid 1980s, using different techniques. Deming et al. (1989) have looked for oscillation signature in thermal infrared. Unfortunately, their infrared detectors, not sensitive enough, did not detect any signal. Oscillations were also sought in velocity measurements, obtained by Doppler spectrometry. Schmider et al. (1991, hereafter S91) used the sodium cell spectrometer and Mosser et al. (1993, 2000, hereafter M93 and M00) the Fourier transform spectrometer FTS (at CFHT, Hawaii) at fixed optical path difference. An excess of power was revealed in the spectrum in the frequency range [0.8−2] mHz, as well as the large separation of oscillation p-modes around 140 μHz. Nevertheless, the oscillation modes have never been individually identified, hindering any constraint on the internal structure.

SYMPA, whose concept and performance have been described in Paper I (Schmider et al. 2007), is an instrument dedicated to Jovian oscillations. For the first time, a specific instrument dedicated to Jovian oscillations was developed, including the necessary imaging capability. Indeed, full disc observations do not allow to distinguish modes of degree higher than 3. The instrument, a Fourier tachometer, is composed of a Mach-Zehnder interferometer that produces four images of the planet in the visible range corresponding to three Mg solar absorption lines at 517 nm. The combination of the four images, in phase quadrature, allows us to retrieve the phase of the incident light, which is related to the Doppler shift generated by the oscillations.

Two instruments were built at Laboratoire Fizeau (Nice University). Three campaigns were carried out simultaneously at two sites: in 2003, at San Pedro Martir (Mexico) and Calern (France) observatories, in 2004 and 2005, at San Pedro Martir and Teide (Canaries) observatories. The 2003 campaign was mainly dedicated to technical commissioning. In the Canaries, bad weather conditions have strongly limited the efficiency of the 2003 and 2004 campaigns, while the 2005 campaign was conducted under better conditions.

In this paper we present the data processing, the real performance and the first results, obtained during the 2005 run at Teide observatory. The processing of the San Pedro Martir data and the combined analysis of both the observing 2005 network campaigns will be considered in a future work. After a short

description of the specificity of Jovian seismological observations (Sect. 2.1) and a presentation of the observing conditions (Sect. 2.2), in Sect. 3 we present the process of data analysis. We describe in Sect. 4 all the steps for an accurate calibration of the data. Sect. 5 presents the data reduction and the obtention of the velocity maps. The analysis of the time series of the velocity measurements obtained during the 2005 run at Tenerife is described in Sect. 6. Section 8 gives on conclusions.

2. Observations

2.1. Specificity of Jovian seismology

Seismological observations require certain specific conditions. First, Jovian oscillations are expected to be strongest in the frequency range [0.5−2.8] mHz (e.g. M00). Oscillation modes with a frequency lower than 0.5 mHz are trapped well below the tropopause; thus, their amplitudes are too low to remain observable at cloud level, where solar light is reflected. Pressure waves with frequency higher than 3 mHz are not trapped in the Jovian interior; thus no oscillation mode can resonate at frequencies higher than this upper limit (Mosser 1995). Consequently, the requirement for the instrument design is that the low frequency noise should be lower than the photon noise for frequencies higher than 0.5 mHz. The thermal response of the instrument has been shown to fullfill this requirement (see Paper I).

Second, the oscillation amplitude has been theoretically estimated by Bercovici & Schubert (1987) to lie between 1 cm s^{-1} and 1 m s^{-1}. From previous observations of S91, M93 and M00, the upper limit of the oscillation amplitude is almost 60 cm s^{-1}. As shown in Paper I, the theoretical performance of the SYMPA instrument is expected to reach 4 cm s^{-1} over a 16-day observation run; this represents a sensitivity gain of a factor of [5−10] with respect to previous observations (S91, M93, M00).

Third, theoretical predictions give a fundamental frequency of about 150 μHz. To a first approximation (asymptotic theory) the successive modes are separated by about this value, and a few hours of observations should be sufficient to separate them. However, the observed spherical harmonics are degenerated by the response of the instrument on the visible side of he planet (Gaulme & Mosser 2005b), therefore each filtered time series corresponding to a given mode includes leakage from the adjacent ℓ and m components. For instance, the separation between $\ell = 0$ and $\ell = 2$ modes would be of the order of 10 μHz and the mean rotational splitting between modes is the inverse of the rotation period of 9 h 55 m, i.e. 28 μHz. However, the fast rotation and the gradient of the vertical density structure of the planet causes a displacement of the components that is no longer equidistant (Provost et al. 1993). As a result of the combination of this different frequency spacing, the frequency spectrum of a given spherical component exhibits a complex structure and could contain several peaks as close as 1 μHz to each other. Therefore a continuous observing period of 10 days would be required to separate those close components without ambiguity.

2.2. Observation conditions

Observations were conducted at Teide observatory (Canaries islands), with the 1.52-m Carlos Sanchez telescope, between March 31st and April 10th 2005. As detailed in Paper I, four images of Jupiter are obtained. Optical parameters inside SYMPA's box are arranged such the four 1.3-arcmin fields cover 128 pixels on the receptor (a DTA CCD, 1024 × 256 pixels). During the run, Jupiter at opposition presented a diameter of 48 arcsec, corresponding to 69 pixels on the CCD camera.

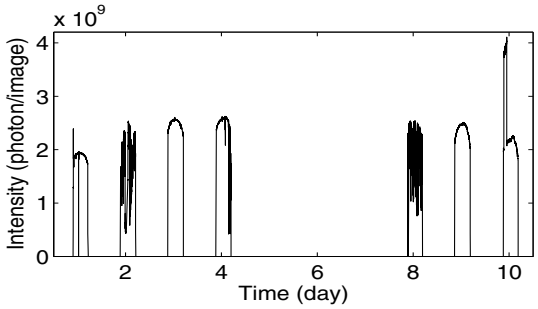

Fig. 1. Total intensity of each image. Nights 2 and 8 and the end of night 4 present a strongly and rapidly variable number of photons, because of cloudy conditions.

Seven nights during the ten day period had good weather conditions, yielding to 23% duty cycle. Data quality was almost constant from one night to another, except for night 2 and 8, where clouds reduced the incident flux. Observation conditions are summarized in Fig. 1 and Table 1. The window function associated with the whole campaign was very strong, since we consider only Canaries data. Therefore, in the power spectrum, the amplitude of a single spike has been divided by a factor 4, since its power is diluted in high side lobes (Fig. 2). The total flux was expected to be about 2.4×10^9 photons per 6-s exposure (Paper I). However, its mean value during the run is about 2.2×10^9 photons per exposure (Fig. 1). This discrepancy with the estimated flux introduces a factor of 0.95 in the ratio of noise value. In Paper I, a noise level of about 4 cm s^{-1} was expected for a 16-night observation campaign, with a 50% duty cycle. Considering only Canaries data, the noise level is expected to be 10 cm s^{-1}.

3. Data processing strategy

3.1. Four interferograms in phase quadrature

SYMPA's instrumental principles are fully explained in Paper I and are summarized in Fig. 3. The four output beams can be described in the detector coordinates (x, y) by the following approximations:

$$I_1(x,y) = \frac{I_0(x,y)}{4}\left[1 - \gamma\cos\phi(x,y)\right] \quad (1)$$

$$I_2(x,y) = \frac{I_0(x,y)}{4}\left[1 - \gamma\sin\phi(x,y)\right] \quad (2)$$

$$I_3(x,y) = \frac{I_0(x,y)}{4}\left[1 + \gamma\cos\phi(x,y)\right] \quad (3)$$

$$I_4(x,y) = \frac{I_0(x,y)}{4}\left[1 + \gamma\sin\phi(x,y)\right] \quad (4)$$

where I_0 is the continuum component of the incident light, that is to say the Jovian figure, γ the fringe contrast and $\phi(x, y)$ the incident wave phase map:

$$\phi(x,y) = 2\pi\sigma_0\Delta(x,y)\left(1 + \frac{v_D}{c}\right) \quad (5)$$

where σ_0 is the central wavenumber of the input filter, $\Delta(x, y)$ is the optical path difference (OPD) and v_D and c are the Doppler and the light velocities. The Doppler shift of the solar Mg lines comes from the combination of the relative motion of Jupiter to the Sun, $v_{J/S}$, the relative motion of the observer to Jupiter, $v_{E/J} + v_{E,rot}$ (distance between the two planets and Earth's

Table 1. 2005 run at Teide observatory.

Starting date m d h m s (UT)	Ending date m d h m s (UT)	Duration h m s	Mean sampling s	Number of acquisitions	Mean intensity photons image^{-1}	Standard deviation photons image^{-1}
Apr.-02, 23:48:14	Apr.-03, 07:03:40	7:09:35	5.45	4727	1.89×10^9	0.67×10^8
Apr.-03, 23:30:14	Apr.-04, 07:02:29	7:31:59	7.13	3792	1.79×10^9	5.27×10^8
Apr.-04, 23:16:12	Apr.-05, 06:58:17	7:39:30	6.75	4080	2.50×10^9	0.76×10^8
Apr.-05, 23:25:29	Apr.-06, 06:50:23	7:22:12	6.68	3971	2.44×10^9	3.80×10^8
Apr.-09, 23:20:17	Apr.-10, 06:31:59	6:37:48	6.28	3799	2.06×10^9	3.62×10^8
Apr.-10, 22:51:11	Apr.-11, 06:33:11	7:41:48	6.33	4376	2.38×10^9	1.14×10^8
Apr.-11, 21:09:35	Apr.-12, 06:30:17	7:20:42	6.83	3872	2.36×10^9	0.97×10^8

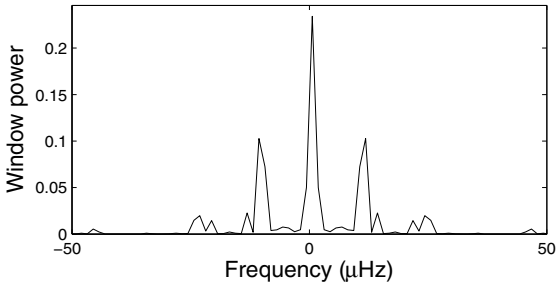

Fig. 2. Spectral window of the observation campaign. The amplitude has been normalized to the spike's power. Only 23% of the total energy remains in the central peak.

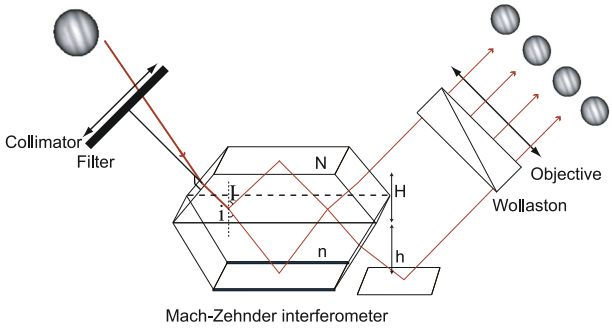

Fig. 3. Schematic view of the SYMPA instrument. The incident light coming from the 1.5-m telescope passes through a 120-mm collimator and the 5 nm bandwidth interference filter. The optical path difference Δ occurs inside the Mach-Zehnder prism; it is a function of the heights H and h, refraction index N and n and incidence angles into the prism I and i: $\Delta = 2(HN\cos I - hn\cos i$. The Wollaston polarizer separates each output from the interferometric device into two separated beams. In total, the instrument produces four images of the same field on the camera, separated by $\pi/2$ in phase (see Paper I).

rotation), Jupiter's rotation $v_{\rm J,rot}$ and, finally the oscillations $v_{\rm osc}$. In the following, we write the Doppler velocity as the sum of:

$$v_{\rm D} = 2\left(v_{\rm J/S} + v_{\rm E/J} + v_{\rm E,rot} + v_{\rm J,rot} + v_{\rm osc}\right). \quad (6)$$

The factor 2 is due to the fact that the Doppler effect is doubled after reflection on Jupiter's atmosphere. The orders of magnitude of these different terms are presented in Table 2.

From Eq. (5), the phase map appears to be the sum of two contributions: a "motionless" term, $2\pi\sigma_0\Delta(x,y)$, and a velocity term, $4\pi\sigma_0\Delta(x,y)v_{\rm D}/c$. The art of extracting the oscillation signal resides in the ability to eliminate step by step the motionless fringes and the "spurious" velocity fields $v_{\rm J/S}$, $v_{\rm E/J}$, $v_{\rm E,rot}$ and $v_{\rm J,rot}$. All the steps of the schematic process in Fig. 3 are detailed in Sects. 4 and 5.

Table 2. Orders of magnitude of different doppler shifts during the 2005 run at Teide observatory.

	Velocity (m s^{-1})
Jupiter-Sun	0.4
Jupiter-Earth	3142
Earth rotation	[−409, 409]
Jupiter rotation	[−12 570, 12 570]
Oscillations	<0.6

3.2. Extracting the oscillation signal

Let us consider a quadruplet of interfering images on the detector's field. The differences between the two pairs of images, which are in phase opposition, allow us to cancel the continuous component of the interferograms I_0, in order to keep the interfering patterns. We write U and V, the normalized interfering patterns:

$$U = \frac{I_1 - I_3}{I_1 + I_3} \propto \gamma\cos\phi \quad (7)$$

$$V = \frac{I_2 - I_4}{I_2 + I_4} \propto \gamma\sin\phi \quad (8)$$

where we drop the (x,y) dependence in order to simplify notation. The incident wave phase is retrieved by taking the argument of the complex interferogram:

$$Z = U + \mathrm{i}V \propto \gamma\,\mathrm{e}^{\mathrm{i}\phi}. \quad (9)$$

The data processing expands in three main steps: correction of the motionless fringes, elimination of Jupiter's rotation and elimination of the relative motion of the observer to the target and of the target to the Sun. Mathematically, it lies in successively creating four complex interferograms, associated with each step of the data processing: Z_0 for motionless fringes, $Z_{\rm J,rot}$ and $Z_{\rm E,rot}$ for Jupiter's and Earth's rotation, $Z_{\rm E/J}$ for the relative motion of the Earth to Jupiter and $Z_{\rm J/S}$ for Jupiter's motion with respect to the Sun. Then, the rough Jupiter complex interferogram $Z_{\rm jup}$ is deconvoluted from the additive signals:

$$Z_{\rm J,flat} = Z_{\rm jup} \times Z_0^* \times Z_{\rm J,rot}^* Z_{\rm E,rot}^* \times Z_{\rm E/J}^* \times Z_{\rm J/S}^* \quad (10)$$

$$\propto \exp\left(\mathrm{i}4\pi\sigma_0\Delta\frac{v_{\rm osc}}{c}\right) \quad (11)$$

where the asterisk indicates the complex conjugation. The resulting interferogram is called $Z_{\rm J,flat}$ because of the appearance of its argument, i.e. the velocity map. Indeed, since oscillation amplitude is expected to be lower than 0.6 m s^{-1}, it is impossible to directly see oscillation modes in a single phase map, where the mean noise level is expected to be about 900 m s^{-1} per pixel (Paper I). Oscillations can be see only in the spectrum of long time series.

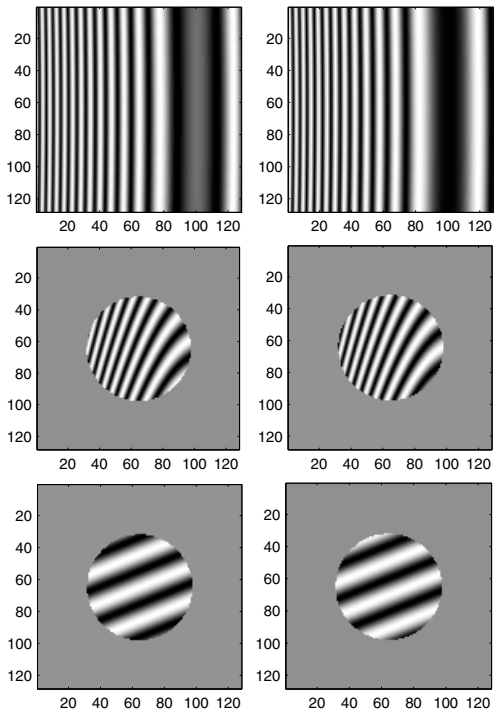

Fig. 4. Simulation of interferograms along the data processing chain. *Top*: motionless interferograms (U_0, V_0). *Middle*: Jovian interferogram $\left(U_{\rm jup}, V_{\rm jup}\right)$ when Jupiter is inclined by $-72°$ with respect to vertical. The interference pattern is mainly due to the coupling between motionless fringes and Jovian rotation (Eq. (6)). *Bottom*: Jovian interferograms deconvoluted from the motionless contribution, $(U_{\rm rot}, V_{\rm rot})$, i.e. fringe pattern associated with Jovian rotation. Note that fringes associated with solid rotation present velocity iso-values parallel to the rotation axis. A differential wind profile has not been introduced.

Note that Doppler shifts due both to the Earth motion relative to Jupiter and Jupiter's motion relative to the Sun are uniform across the field. On the contrary, the Jovian Doppler component is very sensitive to Jovian rotation since its value varies from $-12.57\ \mathrm{km\,s^{-1}}$ to $12.57\ \mathrm{km\,s^{-1}}$ from east to west on the Jovian equator. In terms of velocity, it implies that the error in positioning the phaser $Z_{\rm J,rot}$ must be smaller than the photon noise. Therefore, it requires us to know Jupiter's position to better than 1/20 th of a pixel. Figure 4 presents simulations of the motionless interferograms, Jovian interferograms and the Jovian rotation interference pattern.

4. Data calibration

4.1. Pre-processing operations

Pre-processing consists of cleaning each quadruplet of Jovian images (I_1, I_2, I_3, I_4) to create pairs of interferograms (U, V). This implies three main operations. First, the camera dark current contribution has to be subtracted by using offset images. Second, the inhomogeneities of the single pixel responses to light intensity (photon/electron gain) have to be compensated for by dividing each image by a flat field image. Third, the construction of the Jupiter phase map, using the argument of the complex image created by the difference of two pairs of images, requires that all the four images overlap one to each other. The two first points are easy to obtain, but the last one is difficult because of the required accuracy of about 1/20 pixel.

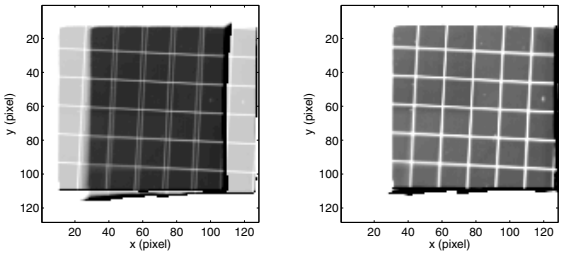

Fig. 5. Overlapping of grids 1 and 3, before and after distortion rectification. The position of the horizontal and vertical lines are determined by fitting the zeros of the grid image derivatives, along both directions x and y. Second order polynomials are sufficient, since rotation and barrel distortion do not require higher orders. Then, each intersection point coordinates are calculated by solving numerically the four order equation coming from the combination of the vertical and the horizontal line fits. The mean distance between intersections points is equal to 5.32% pixel^{-1}.

As for every optical system including lenses and prisms, field distortion is unavoidable. Although Jupiter was positioned as close as possible to the optical axis, its large diameter involves differential distortions between the four images, making the overlapping impossible. The whole distortion effect is supposed to be composed of only translation, rotation and barrel distortion. This problem has been anticipated by placing a regular grid, engraved on a glass slide, at the instrument focus. The grid intersection positions are used to characterize the distortion (Fig. 5).

Let us consider one image among the quadruplet $I_i(x, y)$, $i \in [1, 4]$, where (x, y) are the detector coordinates (CCD pixels). Because of optical distortion, the image value on the (x_k, y_k) point, $k \in [1, 128]$, actually corresponds to the (x'_k, y'_k) point. The repositioning algorithm must produce for each image I_i an image I'_i, defined in the detector's coordinates, as:

$$I'_i(x, y) \;=\; I_i(x', y'). \tag{12}$$

The distorted coordinates (x', y') are related to the regular detector coordinates by the relations:

$$x' \;=\; x + f(x, y) \qquad \text{and} \qquad y' \;=\; y + g(x, y) \tag{13}$$

where f and g are polynomials expressed as $\sum_k C_k x^j y^{k-j}$, where k is the polynomial order and $j \leq k$. The polynomial coefficients C_k are obtained by minimizing the difference between the intersection point coordinates of the grid associated with the considered image I_i and the intersection point coordinates of the regular grid. The knowledge of the set of distorted coordinates (x', y') is used to build the new rectified image $I'_i(x, y)$, by interpolation of $I_i(x', y')$ on the regular detector coordinates.

Interpolation is realized with a cubic method. In Fig. 5 we present a pair of 2-grid images before and after repositioning. Note that the translation repositioning represents the zero order of the transformation. A way to evaluate the accuracy of the repositioning process is to apply it to the previously repositioned grids; they should overlap (Fig. 5, right). The mean distance between the repositioned intersection points from one grid to another lies in the range $[1/20, 1/15]$ pixel, which almost fulfills the required accuracy.

In order to respect the conservation of the flux, correcting operations have to be processed in the following order: first, subtraction of the offset to the image and to to the flat-field, then rectification of the offset-corrected image and flat-field.

$$I_{\rm pre-processed} \;=\; \frac{\left[I(x, y, T) - O(x, y, T)\right]_{\rm rectified}}{\left[F(x, y, T) - O(x, y, T)\right]_{\rm rectified}} \tag{14}$$

where I indicates the considered image (e.g. Jupiter), O the offset image and F the flat-field image. T stands for the temperature of the camera. Note that as assessing the four output intensities are not strictly equal, no photometric balance has to be performed since it is implicitly done by dividing each image by the flat field.

4.2. Motionless fringe calibration

The next step of data processing is the deconvolution of Jovian complex interferograms $Z_{\rm jup}$ from the motionless interferogram Z_0. Therefore, we have to characterize the motionless phase term $2\pi\sigma_0\Delta(x, y)$ (Eq. (5)). Furthermore, as reported in Paper I, the four output beams are not in perfect phase quadrature: the discrepancies between actual measurements and theoretical expectation are about $\varepsilon = 28°$. This shift compared to quadrature has to be quantified precisely across the whole field (x, y).

The knowledge of the optical parameters of both telescope and instrument permits us to describe the motionless fringes (cf. simulations in Fig. 4), but not their imperfections. Strong constraints on the motionless fringes come from solar light scattered by the telescope dome. Indeed, excluding the spectral Doppler shift, it presents the same spectrum as Jupiter, since 517-nm magnesium lines are solar reflected lines. Moreover such a process enables us to light all the detector surface. Actually, the only difference between motionless fringes and "sky" fringes is the uniform velocity field, introduced mainly by Earth rotation, much less by Sun-Earth distance variation and by undesired thermal effects (see Sect. 6). These parameters are taken into account from the IMCCE ephemeride data base (www.imcce.fr).

6-h long "sky" shots were taken on April 2nd. In order to increase the signal to noise ratio of sky interferograms, images are averaged over one minute intervals, which corresponds to three images. Figure 6 presents one of the 330 pairs of 1-min exposure interferograms. Fringes are well defined and fringe contrast ($\simeq$0.4%) is smaller than expected (0.8%). Unfortunately, it appears that the map of both interferograms are not plane, but show a parabolic curvature. The origin of such a residual signal is explained by the fact that sky shots are taken during the day: some direct light enters the instrument, and does not follow the correct optical path.

A method has been developed to treat this unflatness. Let us take two pairs of interferograms (U, V) and (U', V'), taken at two different dates. The phase difference $\delta\phi$ between them is due to terrestrial motion and temperature variation. Their expressions are given by:

$$U = U_0 + \gamma_U \cos(\phi) \qquad U' = U_0 + \gamma_U \cos(\phi + \delta\phi) \tag{15}$$

$$V = V_0 + \gamma_V \sin(\phi + \varepsilon) \quad V' = V_0 + \gamma_V \sin(\phi + \delta\phi + \varepsilon) \tag{16}$$

where (U_0, V_0) describe the unflatness, and (γ_U, γ_V) the fringe contrasts. The subtraction of these signals eliminates the "lack of flatness" terms and brings to the two interfering patterns:

$$\Delta U = U' - U = -\gamma_U \left[2 \sin\left(\frac{\delta\phi}{2}\right)\right] \sin(\varphi) \tag{17}$$

$$\Delta V = V' - V = \gamma_V \left[2 \sin\left(\frac{\delta\phi}{2}\right)\right] \cos(\varphi + \varepsilon) \tag{18}$$

where φ is the mean phase $\varphi = \phi + \delta\phi/2$. Figure 7 shows cuts of $(\Delta U, \Delta V)$ along the x-axis; the unflatness problem has been corrected. The fringe contrast presents optimized variations across both fields, from 0.2% to 0.6%.

The motionless complex interferogram $Z_0 = U_0 + \mathrm{i}V_0$ is obtained by fitting both quadrature shift and phase on the pair $(\Delta U, \Delta V)$. First, the plot of one of the interference patterns as a function of the other highlights the phase quadrature imperfections (Fig. 8). In the case of perfect quadrature and uniform contrast in both interferograms, points would be distributed around a circle centered on 0. As a result, points are distributed

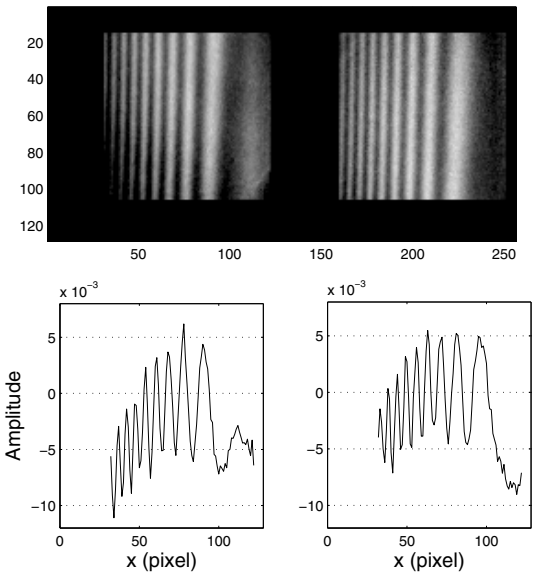

Fig. 6. *Top*: interference pattern (U, V) obtained with solar light scattered by the telescope dome, over one minute (sum of 3 images). *Bottom*: cut along the x-axis of U and V, at the $y = 55$ pixel. Note that both interferograms present a varying contrast between 0.3 and 0.5% and a significant unflatness. Moreover, they are not centered around 0, makes the phase $\phi = \arg(U + \mathrm{i}V)$ impossible to recover.

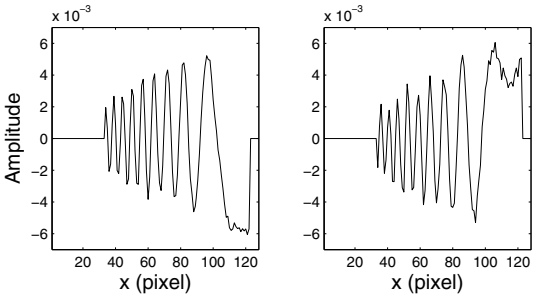

Fig. 7. Cut of interference patterns $(\Delta U, \Delta V)$ along the x-axis. After correction of the low spatial frequency term, fringe contrast still varies strongly, from 0.2% to 0.6%.

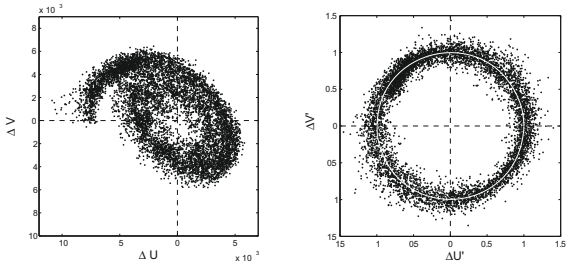

Fig. 8. *Left*: interference pattern ΔU as a function of the other ΔV. The spiral structure comes from the fact that both fringe contrast and ellipticity vary across the field. *Right*: plot of the interference pattern $\Delta U'$ as a function of the other $\Delta V'$. Points are distributed in a circle (solid line, white), which indicates that the two interferograms are in phase quadrature. In terms of phase accuracy, the standard deviation of these points is 5.3°.

along an ellipse whose radius varies strongly on the detector field. The phase shift ε with respect to quadrature is related to the ellipse parameters (A, B) by:

$$\varepsilon = \arcsin\left(\frac{A^2 - B^2}{A^2 + B^2}\right). \quad (19)$$

Since ellipticity and amplitude vary across the field (Fig. 8, left), a further correction has to be applied. Therefore, the field (x, y) is divided in 10-pixel large squares, in which all these parameters are considered as uniform. Ellipse axes are estimated by least square fitting. The resulting parameter estimates (A, B), obtained for each sub-region, are interpolated for each pixel by fitting their values by a 4th order polynomial. Thereafter, using A, B and ε, the amplitude of both interference patterns $(\Delta U, \Delta V)$ are normalized to 1 and the phase shift is set to 90°, by the operation:

$$\Delta U' = \frac{\Delta U_{\rm norm}\cos(\varepsilon/2) - \Delta V_{\rm norm}\sin(\varepsilon/2)}{\cos(\varepsilon/2)} \quad (20)$$

$$\Delta V' = \frac{\Delta V_{\rm norm}\cos(\varepsilon/2) - \Delta U_{\rm norm}\sin(\varepsilon/2)}{\cos(\varepsilon/2)} \quad (21)$$

where the subscript "norm" indicates that amplitudes have been normalized to 1. These new variables are now in the required quadrature. Figure 8 (right) shows the plot of the interference pattern $\Delta U'$ as a function of the other $\Delta V'$; phase quadrature is reached. The motionless phase $\phi_{\rm instru}$ is obtained by fitting the argument of the complex interferogram $Z_{\rm sky} = \Delta U' + {\rm i}\Delta V'$ with a 4th order polynomial. The resulting phase standard deviation is about 5.3°.

The motionless interferogram used in the following to process Jovian data is simply built as:

$$Z_0 = {\rm e}^{{\rm i}\phi_{\rm instru}}. \quad (22)$$

Indeed, since only the phase term matters, the fringe contrast is set equal to 1 in the whole field.

5. From four Jupiter images to a velocity map

Processing the data involves turning each quadruplet of Jovian images into a calibrated radial velocity map. The first step, discussed in the previous section, gives clean fringes in both interference patterns $(U_{\rm jup}, V_{\rm jup})$, in order to create the complex Jovian interferogram $Z_{\rm jup}$. Second, the motionless phase is deconvoluted to $Z_{\rm jup}$ with Z_0 (Eq. (22)). Third, Jovian rotation and other uniform velocity drifts have to be deconvoluted, in order to extract the velocity map.

5.1. Cleaning Jovian fringes

Let us consider a quadruplet of 4 pre-processed Jovian images. Since they have been corrected flat field and optical distortion, each pair of images (I_1, I_3) and (I_2, I_4) present the same intensity level and will overlap (Fig. 9). Then, the two interfering patterns $(U_{\rm jup}, V_{\rm jup})$ are created following Eqs. (7) and (8). Moreover, they are set in phase quadrature following relation (20) and (21). As it can be seen in Figs. 10 interference fringes appear, but, as for the "sky" interferograms, the fringes do not oscillate around 0, but around a distorted surface. These features are photometric residues, which have not disappeared with operations (7) and (8). However, fringes have to be repositioned around a flat surface, centered at 0, in order to follow the phase of the Doppler signal.

The best way to separate the photometric noise and spurious signal is to filter in the spatial frequency domain. The two dimension fast Fourier transform (FFT) is applied to the complex interferogram $Z_{\rm jup}$. In order to avoid spectral leakage due to the finite

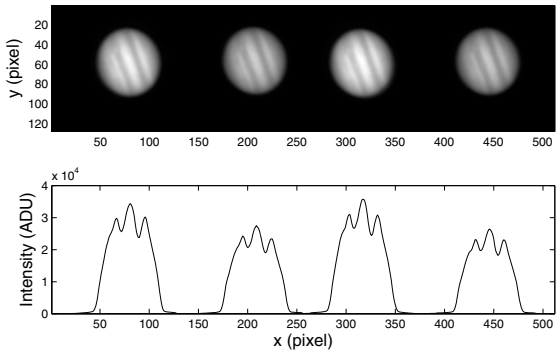

Fig. 9. *Top*: quadruplet of Jupiter images (I_1, I_2, I_3, I_4), taken during the night of April 2nd 2005 at the Teide observatory. *Bottom*: cut of the top images. The instrument exhibits a global polarization effect, resulting in a better transmission of one channel than the other.

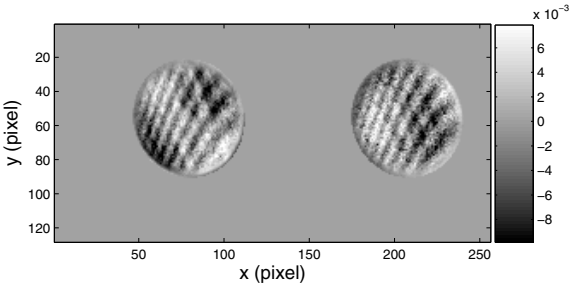

Fig. 10. Rough interferograms $(U_{\rm jup}, V_{\rm jup})$ obtained following Eqs. (7) and (8). The interference pattern is clearly visible, but some photometric residuals of the same order of magnitude as the fringe's contrast, related to Jovian bands and zones, still remain.

size of the image, we apply an oversampling, by a factor 2, on the data $Z_{\rm jup}$ before moving to the Fourier domain. Also, Jupiter's boundary is apodized with a $\cos^3$ function, to avoid Airy-like rebounds due to the Fourier transform. In Fig. 11, we present the Fourier transform modulus. The central region contains the low frequency information (mean value, slow distortions). The horizontal line corresponds to the interference pattern; the horizontal structure comes from the fact that optical path difference varies with the x-coordinates. The inclined alignment of stains constitutes the photometric effect. Indeed, it corresponds to the spatial frequencies along the rotation axis of Jupiter, which is inclined by about −72° in the detector's field. These features are remnants of cloud zones and belts.

Wiener filtering stipulates that the signal can be filtered out from the noise in the Fourier domain if they are clearly differentiable. As can be seen in Fig. 11, fringes occupy distinct positions to photometric residues. Actually, for high degree modes, a coupling between photometric noise and oscillation signal still exists, since high degree spherical harmonics extend widely in the Fourier domain. Therefore, part of the energy in the highest spatial frequencies may be filtered during this operation. Nevertheless, higher frequency mode information will be still available, since most of its signal is not cancelled by filtering operations, but may suffer from amplitude estimate uncertainty.

In order to limit the damage generated by filtering the noise, the spatial filter is as smooth as possible. It consists of an ellipse, whose major axis inclined by −72° with respect to vertical and which includes only the photometric remnants and the central region. As for Jupiter, the filter's boundary is apodized to avoid rebounds by applying the inverse Fourier transform, when returning to the image plane. The resulting pair of interference

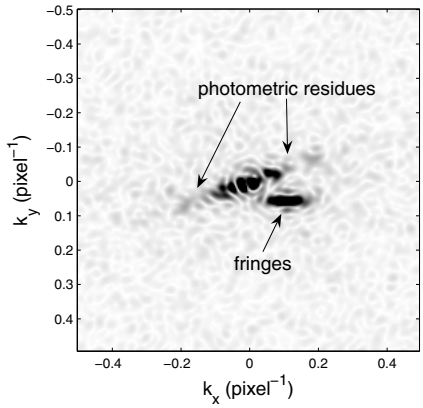

Fig. 11. Modulus of the the Fourier transform of the complex interferogram $Z_{\rm jup} = U_{\rm jup} + {\rm i}V_{\rm jup}$. Photometric residuals are located along the direction indicated by the two upper arrows. This direction fits with Jupiter's inclination in the detector's field. The main fringe information lies in the horizontal line, under the central region.

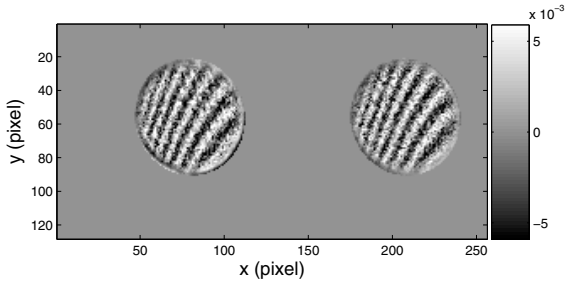

Fig. 12. The same pair of interferograms after filtering of the photometric residuals. Note that fringes oscillate around 0, and that contrast is about 0.6%, which is very close to expected values.

patterns after spatial filtering is presented in Fig. 10. Now, fringes are centered around the 0 value. Hence, the requirements for deconvoluting the motionless phase are met.

5.2. Jupiter velocity map

The motionless fringe deconvolution is realized by the following operation:

$$Z_{\rm j,rot} = Z_{\rm jup} \times Z_0^*. \tag{23}$$

The resulting interference pattern presents fringes parallel to the planetary rotation axis (Fig. 13). Indeed, the projection of Jupiter's velocity field $v = \Omega R(L)$, where Ω is the angular velocity and L the latitude, towards the observer reduces to $v = \Omega x$, where x is the abscissa along Jupiter's equator. At zero order, Jovian rotation can be considered as solid rotation since differential rotation with respect to solid-body rotation is about 1% at the equator. Thus, Ω is almost uniform on the Jovian disk, and the phase of the complex interferogram presents iso-values along the rotation axis. Moreover, since the noise level is about 900 m s^{-1} per pixel, differential rotation is definitely invisible in a single image.

Hence, a complex phaser that reproduces the solid rotation is applied to each Jovian complex interferogram; it is defined by $Z_{\rm solidrot} = \exp(4\pi\sigma\Delta v_{\rm rot}/c)$, where $v_{\rm rot} = 2\pi/T$ and where T = 9 h 55 m 30 s (system III) is the mean rotation period. The main difficulty of such a process is the accuracy of the estimate of Jupiter's position on the detector, because 1 pixel corresponds to 350 m s^{-1}. Two methods have been envisioned to make the

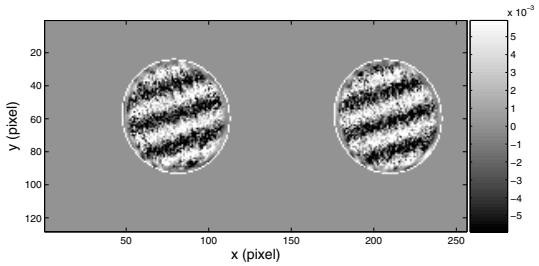

Fig. 13. Interference pattern after deconvolution of the motionless component. Fringes present iso-values along the rotation axis of Jupiter. The white circle indicates Jupiter's size before resizing.

center of the solid rotation phaser $Z_{\rm solidrot}$ overlap the center of Jupiter's interferogram $Z_{\rm j,rot}$. In both cases, a threshold is applied to each image, in order to remove spurious photometric signals, such as Jovian satellites of terrestrial atmospheric light scattering. The "barycenter" method consists of taking the coordinates of the barycenter of the total photometric image $I = \sum_{i=1}^{4} I_i$. The "interspectrum" method consists of determining the relative distance between two images, taken at different dates, by measuring the phase Φ of the interspectrum of the two images. Indeed, the phase of the interspectrum of the pair of images (I_1, I_2) is defined as:

$$\Phi = \arg\{\mathcal{F}(I_1) \times \mathcal{F}(I_2)^*\} \tag{24}$$

$$\propto (x_2 - x_1) + (y_2 - y_1) \tag{25}$$

where (x_1, y_1) and (x_2, y_2) are the coordinates of the center of Jupiter and $\mathcal{F}$ and $\mathcal{F}^*$ indicate the Fourier and inverse Fourier transformations. The second method has been preferred because the barycenter estimate is too sensitive to high spatial frequency photometric details, which vary during the night, such cloud features or satellite transits. On the contrary, the interspectrum method is sensitive only to low spatial frequency.

After deconvolution of the Jovian mean rotation (i.e. the solid body approximation), interferograms become flat since the remaining phase $\phi = 4\pi\sigma\left(v_{\rm J/S} + v_{\rm E/J} + v_{\rm E,rot} + v_{\rm osc}\right)$ is uniform across the field (Fig. 14). The subtraction of $v_{\rm J/S}$ and $v_{\rm E/J}$ is discussed in the next section, since they do not change the signal to noise ratio of the phase map. Therefore, the velocity map is retrieved with Eq. (6) in Paper I:

$$v = v_0 \arg\{Z_{\rm flat}\} \tag{26}$$

with $v_0 \simeq 1$ km s^{-1}. Note that because of apodization created by spatial filtering of photometric residuals, the entire phase map is not exploitable. A part of the external region is reduced, whose proportion is a function of the apodization strength. Here, an external ring representing 1/4 of the Jovian radius is taken away (Fig. 14). As a consequence, the flux is reduced by about 43% of the photons, which makes the expected noise level increase to around 10.5 cm s^{-1}. However, the performance decrease is limited by the low weight of external regions in the Doppler signal.

The standard deviation of velocity across the Jovian disk is about 890 m s^{-1} per pixel, that is to say 18.9 m s^{-1} when integrating the 2200 pixels of the resized Jovian disk. This performance matches expectations. If photon noise is reached, a 7-h night integration with 6-s sampling yields a noise level as low as 29 cm s^{-1}.

6. Temporal analysis over one night

In the previous section, we have presented the data processing method for a single Jupiter quadruplet, for the extraction of the

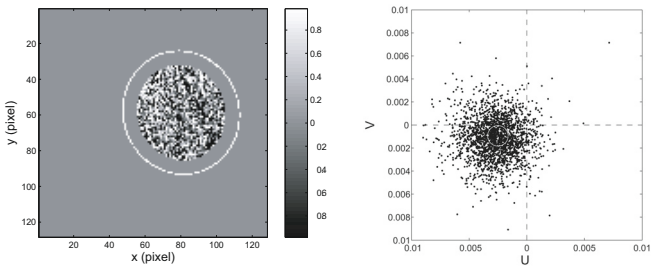

Fig. 14. *Left*: Jupiter phase map, after deconvolution of motionless phase and Jovian rotation. Terrestrial motion and temperature variations have not been taken into account, since they only shift the whole phase by a uniform value. *Right*: complex diagram of the same interferogram; $V_{\rm flat}$ is plotted as a function of $U_{\rm flat}$. The white circle indicates the standard deviation of the phase of the interferogram, whose value is 8.9×10^{-4} rad. In terms of velocity, it corresponds to 890 m s^{-1} per pixel, 18.9 m s^{-1} on the whole disk (2200 pixels after resizing).

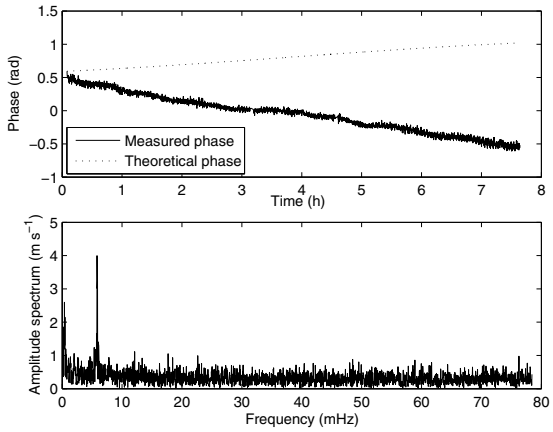

Fig. 15. *Top*. Median phase over night 9: measured phase (full line) versus theoretical phase drift due to Earth rotation and relative motion of Jupiter toward the Sun and the Earth (dashed line). *Bottom*. Amplitude spectrum of the measured phase as a function of the time frequency. Two spike forests exceed the mean noise level at less than 0.5 mHz and at 6 mHz. Note that the mean noise becomes flat in the frequency range above 20 mHz, which means that photon noise is reached, around 41 cm s^{-1}.

Doppler signal. In this section, we analyse the time series of the median phase extracted for each Jovian quadruplet. Then, we identify the different sources of noise and present correction methods.

6.1. Phase global behavior

The study of the median phase over a single night allows us to evaluate the mean noise level and to identify spurious signals. Median phases are extracted from Jupiter's flat interferograms $Z_{\rm flat}$ as follow:

$$\phi_{\rm med} = \arctan\left(\frac{V_{\rm med}}{U_{\rm med}}\right) \tag{27}$$

where the subscript "med" indicates the median value of the considered variable. This estimate of Jupiter's median phase has been preferred to the direct median of the phase map, in order to avoid noise coming from 2π jumps (see Fig. 14). In Fig. 15, the median phase over night 9 and its power spectrum have been plotted.

First, according to data processing chain (Eqs. (5), (10) and (11)), phase measurement is proportional to the redshift of spectral lines. It appears that the signal is overwhelmed by strong low frequency noise. Indeed, over the night, the velocity variation should be dominated by the Earth rotation (409 m/s amplitude at Teide observatory), so the phase should increase by about 0.41 rad instead of decreasing by about 1.12 rad. This implies that an unexpected stronger low frequency drift dominates. Besides this low frequency noise, the power spectrum highlights a rapid oscillation noise source around 6-mHz frequency.

The standard deviation of the median phase is around 27 m s^{-1} per image; images were taken every 6 s. By supposing an only photon noise origin, the noise level reduces to 15 cm s^{-1} for 7 nights of 7 h, which is 1.3 time worse than expected from the previous section. In the following subsections, we interpret the noise origins and describe the method that has been used to remove their main effects.

6.2. Temperature effect

Paper I described that the interferometer is made of two pieces of two different glasses, specially chosen to compensate for the index variations and the dilatation, in order to have a stable OPD. In particular, a temperature variation of about 1°C should have no effect on the OPD in a 14°C environment.

The median of Jupiter's median phase over each night has been plotted as a function of the corresponding median temperature (Fig. 16). Phase and temperature appear clearly correlated. A variation of 1°C introduces a phase shift of 0.33 rad (i.e. 330 m s^{-1}), which is much above the expected value (between -60 m s^{-1} and 30 m s^{-1} for the temperature between 0 and 20°C; see Paper I). In fact, such a thermal effect is retrieved when taking into account the error bars on the dilatation coefficient and refractive index thermal dependance (±10%).

Unfortunately, the correlation coefficient reported in Fig. 16 does not allow us to correct the Jovian phase map of its thermal dependence. Indeed, the comparison of phase and temperature over one night does not match correctly: a several hour delay is still present (Fig. 17). This discrepancy is due to the fact that temperature measurements do not correspond to the Mach-Zehnder prism, but to the metallic box in which it lies. Because of a greater thermal inertia, actual glass temperature is time-shifted with respect to the metal temperature. Therefore, a low frequency filter is applied to the data in order to reduce the noise in the frequency range below 0.2 mHz.

Beyond a mean OPD drift, temperature variations generate differential OPD variations with respect to light incidence angle onto the prism. Since Jovian interferograms are deconvoluted from motionless fringes with the help of a constant interferogram (Eq. (23)), the differential OPD variations introduce a slowly varying inclined surface in the Jovian flat phase maps (Fig. 18). This surface is bent along the x-axis because the OPD is only x-dependent. Such an inclined surface yields a high frequency perturbation correlated to Jupiter's position in the observed field. This noise is reduced by fitting the spurious surface on each phase map, by a plane inclined only with respect to the x-axis. Thereafter, Jupiter's phase map is set flat by using a smoothed estimate of the fitted parameters.

6.3. Guiding noise

The so-called "guiding noise" is the perturbation related to Jupiter's position, which should not occur if Jupiter were at a fixed position. Theoretically, SYMPA's Doppler velocity measurements are not sensitive to Jupiter's position on the field,

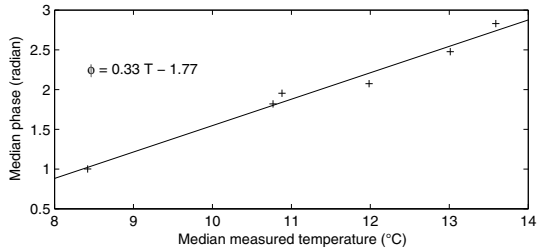

Fig. 16. Phase-temperature correlation. For each night, we plot the median of the median phase as a function of the median temperature over the entire night. The straight line represents the least square estimate of the correlation between phase and temperature.

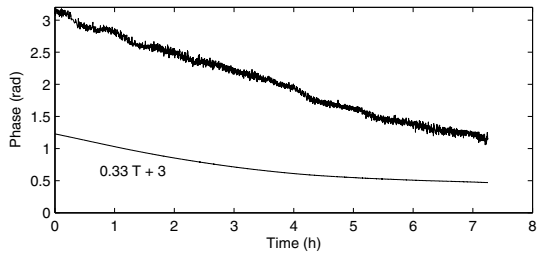

Fig. 17. Jovian median phase, corrected for the Earth's rotation component, over night 10 (full noisy line) and temperature converted to phase with the previously fitted correlation coefficient (full smooth line). Note that the measured phase follows the temperature with a several hour delay.

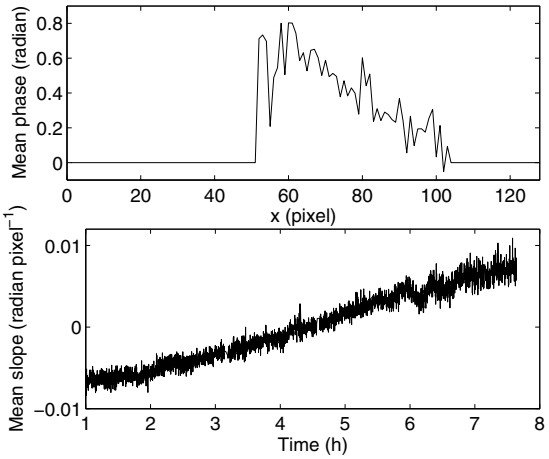

Fig. 18. *Top*: phase map averaged along the y-axis as a function of the x-axis. A negative slope is clearly visible. *Bottom*: root mean square estimate of the slope of the inclined plane along night 10.

because after motionless fringe deconvolution (Eq. (23)) nothing should depend on the coordinates. However, the comparison between spectra of Jupiter's phase and coordinates (x, y) (Figs. 15 and 19) shows a strong correlation at 6 mHz. In fact, many other correlated signatures occur at many frequencies.

This guiding noise has two main origins. First, the temperature high frequency noise cannot be totally cancelled because of the inclined surface fit inaccuracy. Second, Jupiter's position is estimated around 1/15 of pixel. Therefore, the deconvolution of Jovian rotation introduces a spurious signal correlated to Jovian position. Thus, the guiding noise is a combination of these two effects, for which it is hard to determine which of them predominates.

The guiding noise is strongly reduced by removing the intercorrelation of Jupiter's phase and coordinates. The decorrelated

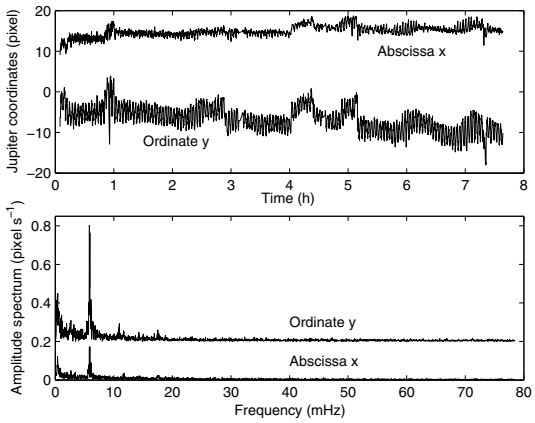

Fig. 19. *Top*. Jupiter's coordinates (x, y) in the CCD field over night 9. Note that y varies much more than the x coordinate because Jupiter is rotated about −72° on the image and because most of the telescope guiding problems occur with the right ascension. *Bottom*. Amplitude spectrum of both coordinates. They present strong components below 6 mHz and significant spikes up to 18 mHz.

phase with respect to both coordinated $\phi_{\mathrm{decorr/x/y}}$ is obtained as follow:

$$\phi_{\mathrm{decorr/x}} = \mathcal{F}^{-1}\{(1 - I_{\mathrm{x}})\mathcal{F}\{\phi\}\} \quad (28)$$

$$\phi_{\mathrm{decorr/x/y}} = \mathcal{F}^{-1}\{(1 - I_{\mathrm{y}})\mathcal{F}\{\phi_{\mathrm{decorr/x}}\}\}. \quad (29)$$

where $\phi_{\mathrm{decorr/x}}$ indicates the phase decorrelated with respect to x, and I_{x} and I_{y} the interspectra relative to x and y, defined by:

$$I_{\mathrm{x}} = \frac{2}{\pi}\frac{\arcsin\left(\Re\{\mathcal{F}(\phi)\mathcal{F}^{*}(x)\}\right)}{|\mathcal{F}(\phi)||\mathcal{F}^{*}(x)|} \quad (30)$$

$$I_{\mathrm{y}} = \frac{2}{\pi}\frac{\arcsin\left(\Re\{\mathcal{F}(\phi_{\mathrm{decorr/x}})\mathcal{F}^{*}(x)\}\right)}{|\mathcal{F}(\phi_{\mathrm{decorr/x}})||\mathcal{F}^{*}(x)|}. \quad (31)$$

Note that we apply a 75% threshold upon I_{x} and I_{y} in order to decorrelate only significant guiding noise spikes.

Jupiter's phase standard deviation drops from 27 m s^{-1} per image to 21 m s^{-1}, which is very close to the expected photon noise level (19 m s^{-1} per image). Hence, by supposing that the remaining noise is only due to photons, the noise level reduces to 32-cm s^{-1} in a 7-h integration and to 12 cm s^{-1} after 7 nights. The remaining non-photon noise is ignored.

7. The search for oscillations: no evidence for a Jovian signal

7.1. Decomposition into the spherical harmonic base

A stationary oscillation mode can be described as the sum of two spherical harmonics of degree ℓ and order $\pm m$. The Jupiter velocity field related to p-modes follows such a description. Therefore, the Doppler signature of the radial velocity field expands on a base made of the projected complex spherical harmonics towards the observer.

The coefficients c_ℓ^m associated with each spherical harmonic Y_ℓ^m are obtained as follow:

$$c_\ell^m = \frac{\sum_{\mathrm{pixels}} \Re\{Y_\ell^m\} \times v}{\sum_{\mathrm{pixels}} \Re\{Y_\ell^m\}} + \mathrm{i}\frac{\sum_{\mathrm{pixels}} \Im\{Y_\ell^m\} \times v}{\sum_{\mathrm{pixels}} \Im\{Y_\ell^m\}} \quad (32)$$

where v indicates the velocity map (Eq. (26)). The normalisation coefficient is chosen with respect to the actual number of pixels

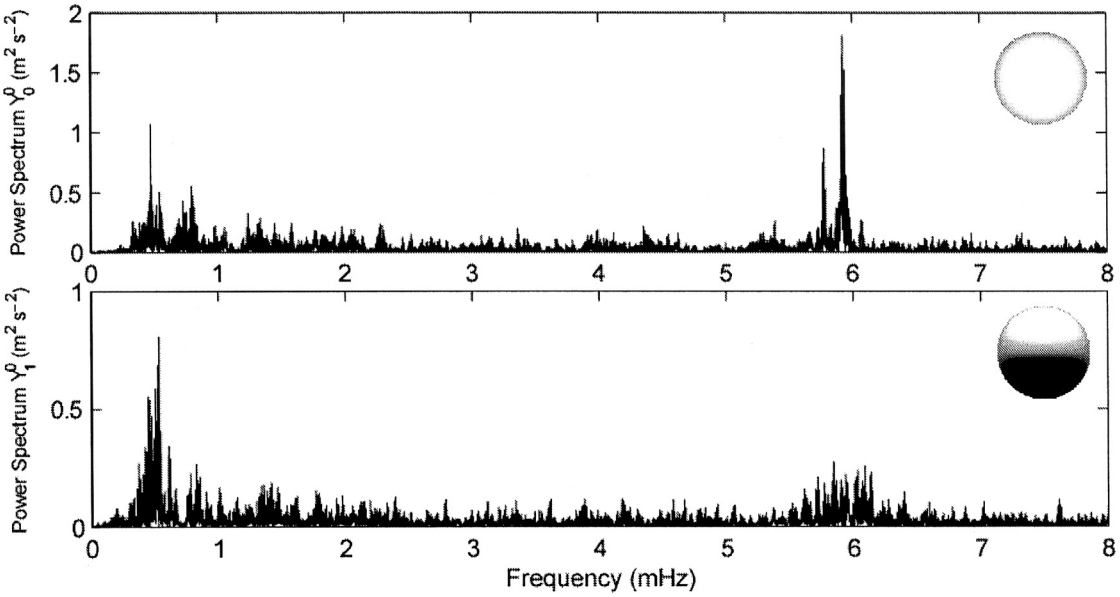

Fig. 20. Power spectrum of the time series related to modes $(0,0)$, *top*, and $(1,0)$, *bottom*, after concatenation of data along the whole run. The mean noise level is respectively of about 12.6 cm s^{-1} and 11 cm s^{-1}, which matches the last estimate of the photon noise. The 6-mHz guiding spike still is about 1.3 m s^{-1} for the $(0,0)$ mode, whereas it is only about 0.5 m s^{-1} for the $(1,0)$ mode.

after resizing. The c_ℓ^m coefficient moduli are expressed in m s^{-1}. The oscillation search is performed in the spectra of all spherical harmonics up to the degree $\ell = 25$.

7.2. Regular temporal grid

Velocity maps are extracted from mean flat interferograms, averaged in 30-s intervals, but calculated every 15 s. Such a process has two reasons. On the one hand, the mean noise level inside the velocity maps drops by a factor of $\sqrt{5}$ since 30 s contains 5 images, which limits strongly the 2π jumps which appear when applying Eq. (26). On the other hand, it allows us to use the fast Fourier transform (FFT) to calculate the power spectra. The procedure is of great interest because the search for modes up to 25 means 625 spectra of 27 000 points in the time series. The spacing of data every 15 s imposes a cut-off frequency at 16.3 mHz, which is well beyond the expected p-modes (less than 3.5 mHz from Mosser 1995). The averaging within 30-s intervals is done in order to avoid spectrum leakage when calculating the Fourier transform.

7.3. Power spectrum of modes $(\ell = 0, m = 0)$ and $(\ell = 1, m = 0)$

We present the power spectrum of the time series corresponding to spherical harmonics Y_0^0 and Y_1^0, for all the data of the Canaries observation campaign. The choice of these two modes among the 625 permits us to present the two main types of spectra. The first is sensitive to the remaining guiding noise, whereas the second is much less sensitive. Indeed, since guiding noise is mainly due to right ascension control defects, the mode $(\ell = 1, m = 0)$ (hereafter $(1,0)$) is less sensitive to these problems since the north and south Jovian hemispheres compensate (Fig. 20).

Both spectra exhibit a flat noise level in the frequency range $[1, 8]$ mHz, except around 6 mHz, where a guiding signal subsists. Beyond 8 mHz, the averaging over 30 s truncates the signal. The guiding signature is reduced from 4 m s^{-1} to 1.3 m s^{-1} after decorrelation. The mean noise level is about 12.6 cm s^{-1} for mode $(0,0)$ and 11 cm s^{-1} for mode $(1,0)$, which is consistent with the last-estimated photon noise level. Note that such a performance has never been reached on Jupiter and proves that the instrument and the data processing chain work efficiently.

As regards the comparison to previous observations of S91 and M93 and M00, no excess of power is present in the $[1,2]$ mHz frequency range. Moreover, no large spacing ν_0 is highlighted, whose value is estimated around 150 μHz, and which was detected around 136 and 143 μHz, respectively, by S91 and M00. Such a difference to previous observations will be analyzed in detail in a future work.

For the excess of power in the frequency range $[0.3, 0.6]$ mHz, no indication for a Jovian origin can be furnished at this step of the data analysis. It could be a remaining low frequency noise, related to temperature and position. A global analysis over all the modes up to degree $\ell = 25$ is required to determine its origin and to highlight the global signature as the Jovian rotation frequency or the ν_0 frequency.

7.4. Global analysis: no evidence for a Jovian signal

As for helioseismology, simultaneous temporal and spatial frequency analysis may reveal the presence of significant information lost among noisy spectra. In Fig. 21 we present the (ℓ, ν) and (m, ν) diagrams. In the (ℓ, ν) diagram, the low frequency excess of power, detected in the $(0,0)$ and $(1,0)$ power spectra, is confirmed for almost all degrees ℓ in the frequency range $[0.3, 1]$ mHz. It does not exhibit an organized structure. Moreover, in comparison to past observations, no signal is distinguishable in the $[1,2]$ mHz range. On the other hand, in the (m, ν) diagram, the same excess of power appears to be strongly structured. The energy is distributed along 2 main lines, symmetric with respect to abscissa, beginning at 0.5 mHz and ending at 1.2 mHz for $m = \pm 25$. Moreover, a second pair of lines, almost parallel to the first ones, is still visible between frequency 0.7 and 1.6 mHz. The mean slope of the principal lines is about 28 μHz, which corresponds to the Jovian rotation frequency.

A quick analysis of the (m, ν) diagram gives some indications. A simple guiding noise origin is excluded, because such a spurious signal contaminates all the eigenmodes at the same

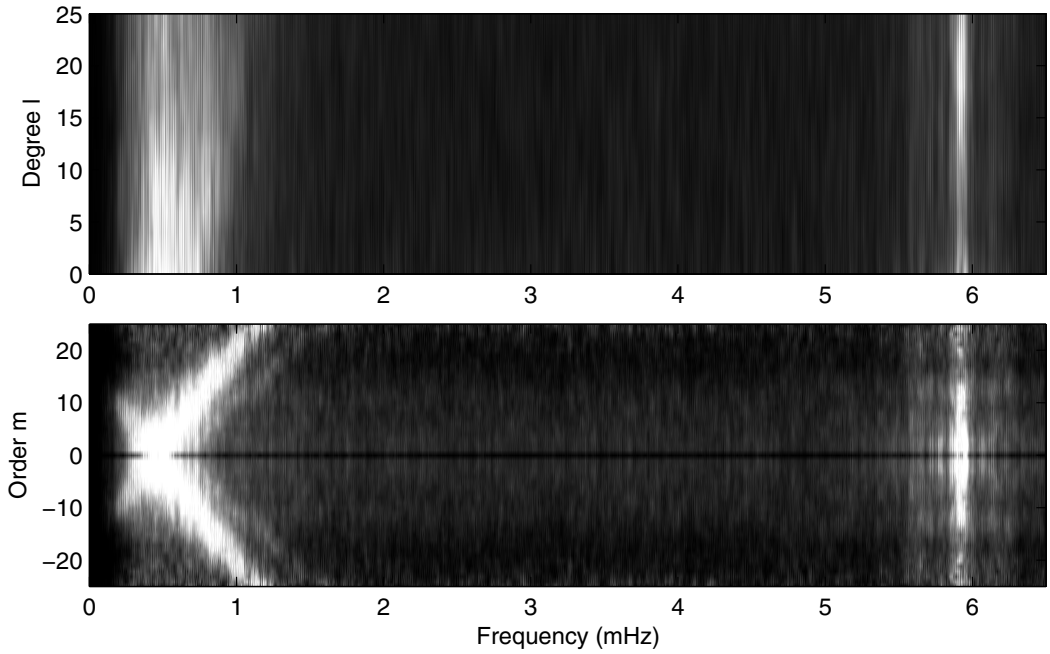

Fig. 21. Time-spatial frequency analysis. *Top*, the (l, ν) diagram represents the mean of all the power spectra at a given degree ℓ, as a function of all the explored degree. *Bottom*, the (m, ν) diagram represents the mean of all power spectra at a given order m, as a function of all explored orders. Note that the guiding noise is still present at 6 mHz, within the vertical line in both graphics. The maximum amplitude is around 1.2 m s^{-1}.

frequency, as for the 6 mHz spike (see Fig. 21). Furthermore, guiding noise becomes negligible beyond order $m = 15$, since its effect compensates when applying high order spherical harmonic filtering to velocity maps. Also, if the slope of about 28 μHz is a chance occurrence, it could indicate a Jovian origin of the observed signal.

However, the Jovian signal hypothesis may vanish by supposing a coupling between two spurious signals. After summation of the velocity maps over 10 min, a fringe structure still remains, whose periodicity fits almost to $m_0 = 16$ (Fig. 22). Also, it can reasonably be supposed that the photometric signal has not been totally removed after the Fourier filtering step (see Sect. 5.1). Thus, a signal modulated by Jupiter's rotation probably underlies in the velocity maps. The coupling of these two spurious signals introduces a modulation of the signal by a $\cos(m_0\Phi)$ factor, where $\Phi = \Omega_r t$ comes from the photometric remnants; $\Omega_r = 2\pi\nu_r$ indicates the Jovian rotation frequency. Consequently, when applying the spherical harmonic search algorithm (Eq. (32)), a coupling appears between the $\cos(m_0\Phi)$ modulation of the velocity maps and the $\cos(m\Phi)$ associated with Y_ℓ^m. With this assessment, velocity maps are modulated in the following way:

$$v = v_D \cos(\Omega_r m_0 t) \cos(\Omega_r m t) \quad (33)$$

$$= \frac{v_D}{2} \{\cos[\Omega_{rot}(m_0 + m)t] + \cos[\Omega_{rot}(m_0 - m)t]\}. \quad (34)$$

Therefore, a linear dependence $\nu = m\,\nu_r + C$ appears, where the constant term $C = m_0\nu_r$ is about 450 μHz, which matches the observed origin of the two lines.

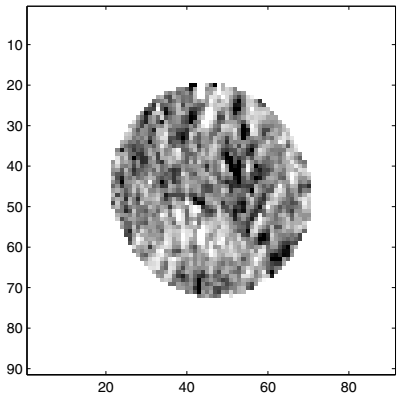

Fig. 22. Velocity maps averaged over 5 min. A fringe structure, inclined at about Jupiter's inclination on the detector, is still present. The coupling of these feature with the spherical harmonic masks may explain the observed features in the (m, ν) diagram.

8. Conclusion and prospects

8.1. Instrument performance

The aim of the SYMPA instrument was the detection and measurement of acoustic modes on the giant planets of the solar system, with a previously unequalled sensitivity around 4 cm s^{-1}. Such a performance was estimated for a 16-day observation campaign with 50% duty cycle (see Paper I). By choosing to process only the Canaries data, since the instrument used at San Pedro Martir Observatory has some defects that make the data more difficult to process, the duty cycle is only 23% over 10 nights. In this case, the noise level is reevaluated at 10 cm s^{-1}. By taking into account the lack of photons by a factor of 2, underlined in Sect. 2.2, the 1σ sensitivity decreases to 12 cm s^{-1}. After decorrelation of the time series with respect to Jupiter's position on the detector, outside the low frequency range ($\leq$0.8 mHz) and the 6-mHz spike, the power spectra are flat and the mean noise level reaches 12 cm s^{-1}. Such a noise level is 5 time better than previous observations which were limited to 60 cm s^{-1} (M00).

However, because of the duty cycle, the effective 1σ velocity sensitivity does not match the noise level. Indeed, it reduces the observed amplitude of any oscillations by a factor of $(0.23)^{0.5}$.

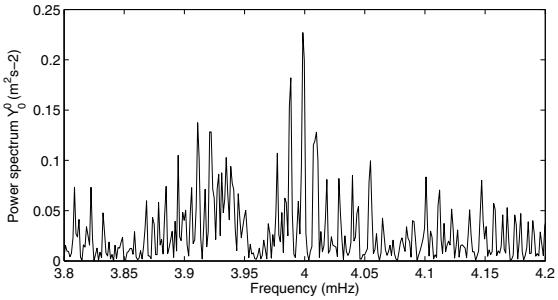

Fig. 23. Magnification of the power spectrum of mode $\ell = 0$ in the frequency range [3.8, 4.2] mHz, where we have introduced a 1 m s^{-1} spurious signal, at frequency $\nu = 4.0$ mHz. Because of the duty cycle the amplitude of the peak is scaled down from 1 m^2 s^{-2} to 0.23 m^2 s^{-2}.

As an example, we checked the effect of the duty cycle and noise level by the introduction of a spurious 1 m s^{-1} amplitude periodic signal at a frequency of 4.0 mHz. The mode is detected with an amplitude of 0.23 m^2 s^{-2} , as a consequence of the duty cycle (Fig. 23). Under these conditions, only a 25 cm s^{-1} signal could be detected at 1σ level.

8.2. The instrument

The data processing has revealed that the instrument is able to reach the photon noise level in most of the explored frequency range. However, it has also highlighted some defects, such the too strong optical path difference dependence on temperature and some difficulties, such the separation between photometric and spectrometric information. The latter make the extraction of Doppler velocity hard to achieve. This is mainly due to an insufficient accuracy in rectifying the distortion, particularly the photometric effect of the distortion (variable PSF upon the detector). This point suggests some instrumental modification, as the time modulation of OPD in order to modulate the phase of the fringe pattern of about π. It would allow us to replace the spatial subtraction between interferograms by a time subtraction. Moreover, the spectral information would be emphasized more easily by narrowing the entrance filter, which would affect the global sensitivity. This would increase the fringe contrast.

8.3. Jupiter

Jupiter seismological observation in S91, M93 and M00 all show an excess of power in the frequency range [1, 2] mHz, which matches theoretical expectations (e.g. Mosser et al. 1996). Moreover, they did not provide any spatial resolution. If both observation methods (sodium cell and Fourier transform spectrometry at fixed OPD) have presented an excess of power in the same frequency range, the large spacing ν_0 estimate was very noisy and differed from the theoretical value of 153 μHz (Gudkova et al. 1995).

Our observations do not present features close to the p-mode signature: the absence of the large spacing ν_0 in power spectra and (ℓ, ν) diagram is significative. However, because of the resizing of the Jovian velocity maps, the projected spherical harmonic base becomes degenerate. Therefore, information from a given mode becomes diluted in other mode spectra, which may strongly diminish the p-mode signature and the identification of specific related structures. A way of dealing with this degeneracy has to be developed.

Bercovici & Schubert (1987) roughly estimated Jupiter's oscillation velocity amplitude to be between a 1 cm s^{-1} and 1 m s^{-1}. Therefore it is to be expected that oscillations are not revealed with a 25 cm s^{-1} effective 1σ velocity sensitivity.

It was impossible to detect solar oscillations in our data. First, the greatest solar oscillation amplitude reached 19 cm s^{-1} for mode $\ell = 0$ and 25 cm s^{-1} for mode $\ell = 1$ (Kjeldsen et al. 2008). Such a velocity is just below the effective 1σ velocity sensitivity taking into account the duty cycle. Second, contrarily to Jupiter, the Doppler shift generated by the solar velocity field is not enhanced by a factor of 2. Therefore, a velocity field of 25 cm s^{-1} on the Sun will produce the same Doppler shift as a 12.5 cm s^{-1} velocity field on Jupiter, which is half the effective 1σ velocity sensitivity.

8.4. Prospects

SYMPA has been demonstrated to work properly, after taking into account its technical defects (temperature dependance, field distortions, difference of intensity between the two polarized outputs, lower sensitivity of the CCD). It has permitted us to obtain the best remote sensing velocity measurements on giant planets. Some improvements are needed on the existing instrument, such a better thermal insulation and a slightly modified optical design in order to reduce the geometrical distortions. An alternative and more efficient solution is to rebuild the prism, equipped with an OPD time modulation.

This seismometer is a tachometer, that furnishes velocity maps, instead of point to point measures, which is the case of echelle-spectrometers. Thus, it can be used for other kind of observations, such as wind velocity measurements. SYMPA tested other extra seismological application in November 2007, by participating in a ground-based observation campaign organised in conjunction with the ESA Venus-Express probe, in order to characterize the lower mesosphere wind velocity.

What future for giant planet seismology? The main obstacles to such measurements are the temporal coverage and atmospheric turbulence. Temporal coverage introduces a windowing effect which makes the signal amplitude decreased and the deconvolution of noise with respect to the signal very hard to perform because of the spreading of information into large frequency ranges. Atmospheric turbulence limits the spatial resolution and, above all, makes the planet move in the field, which generates guiding noise. A significant improvement would arise with Antarctic observations: Schmider et al. (2005) showed that a 80% duty cycle can be reached for more than 3 months. However, oppositions of Jupiter in the southern hemisphere's sky will last in 2009, and afterwards will not occur again until 2018.

The ideal opportunity would come from space measurements aboard an interplanetary spacecraft cruising towards Jupiter. With an optical design similar to SYMPA, a 10-cm entrance pupil observing for 2 months at a mean distance of 0.2 AU to Jupiter would allow us to reduce the noise level to few mm s^{-1} and to increase the spatial resolution until degree $\ell = 100$. Such an instrumental concept has been proposed to the European project of the mission to the Jupiter system, JGO-EJSM, part of ESA's Cosmic Vision programme (Blanc et al. 2006). The concept is derived from the ground based instrument SYMPA and the space helio-seismometer MDI onboard on the SOHO space Solar observatory (Scherrer et al. 1995). It would simultaneously produce intensity maps of reflected solar light, velocity maps and polarimetric maps of the whole visible surface with a spatial resolution of about 500 km at the surface of Jupiter. Also, such an instrument would be an efficient tool to measure the wind velocity of the upper troposphere and the lower stratosphere. Such a

spatial project needs a feasibility study. On one hand, from an instrumental point of view: re the specific requirements of seismology compatible with the interplanetary probe programme? Is the envisioned method the most suitable for space measurements, or should COROT-type photometric measurements (Baglin & The COROT Team 1998) be preferred, as suggested by Mosser et al. (2004) and Gaulme & Mosser (2005a)? On the other hand, theoretical improvements have to be performed on the mode excitation mechanism, in order to evaluate the amplitudes of the expected oscillations.

Acknowledgements. The authors are very grateful to Benoît Mosser for the regular contributions during all the data processing phase and also for the careful reading of the paper.

References

Baglin, A., & The COROT Team 1998, in New Eyes to See Inside the Sun and Stars, IAU Symp., 185, 301
Bercovici, D., & Schubert, G. 1987, Icarus, 69, 557
Blanc, M., Coradini, A., Drossart, P., et al. 2006, in European Planetary Science Congress, 684
Cameron, A. G. W. 1978, Moon and Planets, 18, 5
Deming, D., Mumma, M. J., Espenak, F., et al. 1989, ApJ, 343, 456
Gaulme, P., & Mosser, B. 2005a, Icarus, 178, 84
Gaulme, P., & Mosser, B. 2005b, in SF2A-2005: Semaine de l'Astrophysique Francaise, ed. F. Casoli, T. Contini, J. M. Hameury, & L. Pagani, 155
Gudkova, T. V., & Zharkov, V. N. 1999, Planet. Space Sci., 47, 1211
Gudkova, T., Mosser, B., Provost, J., et al. 1995, A&A, 303, 594
Guillot, T., Stevenson, D. J., Hubbard, W. B., & Saumon, D. 2004, The interior of Jupiter, Jupiter. The Planet, Satellites and Magnetosphere, 35
Kjeldsen, H., Bedding, T. R., Arentoft, T., et al. 2008, ArXiv e-prints, 804
Mayer, L., Quinn, T., Wadsley, J., & Stadel, J. 2002, Science, 298, 1756
Mosser, B. 1995, A&A, 293, 586
Mosser, B., Galdemard, P., Lagage, P., et al. 1996, Icarus, 121, 331
Mosser, B., Gaulme, P., & The Jovis Team 2004, in SF2A-2004: Semaine de l'Astrophysique Francaise, 83
Provost, J., Mosser, B., & Berthomieu, G. 1993, A&A, 274, 595
Safronov, V. S., & Ruskol, E. L. 1982, Icarus, 49, 284
Scherrer, P. H., Bogart, R. S., Bush, R. I., et al. 1995, Sol. Phys., 162, 129
Schmider, F. X., Jacob, C., Fossat, E., et al. 2005, in EAS Pub. Ser., 285
Schmider, F. X., Gay, J., Gaulme, P., et al. 2007, A&A, 474, 1073